Journal of Power Sources 195 (2010) 5213–5227

Contents lists available at ScienceDirect

Journal of Power Sources

journal homepage: www.elsevier.com/locate/jpowsour

Numerical investigation of the impact of gas and cooling flow configurations on current and water distributions in a polymer membrane fuel cell through a pseudo-two-dimensional diphasic model

Sylvain Chupin[a,b], Thibaut Colinart[c], Sophie Didierjean[a,*], Yves Dubé[b], Kodjo Agbossou[b], Gaël Maranzana[a], Olivier Lottin[a]

[a] Laboratoire d'Energétique et de Mécanique Théorique et Appliquée, UMR 7563 CNRS–INPL–UHP, 2, avenue de la forêt de Haye, BP 160, 54504 Vandoeuvre lès Nancy Cedex, France
[b] Institut de Recherche sur l'Hydrogène, Université du Québec à Trois-Rivières 3351 boul. Des Forges, C.P. 500, Trois-Rivières, QC, Canada G9A 5H7
[c] Laboratoire d'Ingénierie des MATériaux de Bretagne (LIMATB), EA-4250, Université Bretagne Sud, IUT de Lorient Allée des pommiers 56300 Pontivy, France

ARTICLE INFO

Article history:
Received 16 November 2009
Received in revised form 2 March 2010
Accepted 6 March 2010
Available online 15 March 2010

Keywords:
PEM fuel cell
Water management
Two-phase flow
Modelling
Current distribution
Catalyst layer

ABSTRACT

For optimal performances, proton exchange membrane fuel cells require fine water and thermal management. Accurate modelling of the physical phenomena occurring in the fuel cell is a key issue to improve fuel cell technology. Here, an analytic steady state diphasic 2D model of heat and mass transfer is presented. Through this model, the aim of this work is to study the influence of local events on the global performances of a fuel cell. A part of the complete model is a microscopic representation of the coupling between water transport and charge transfers in the electrodes. The thickness of the liquid layer around the reactive agglomerates is deduced from the saturation. The evolution of the quantity of water within the catalyst layer is monitored and its influence on the global performances of the cell is investigated. In gas diffusion layers (GDLs), liquid and vapour water transport through are computed regarding the temperature. The flow direction of cooling water modifies the current density distribution along the cell. The impact of the direction of air and hydrogen feeding channels are investigated. It can modify greatly the fuel cell mean current density and the net water transport coefficient. The counter-flow mode was preferable. Likewise, thanks to a better membrane hydration, it results in independent performances regarding the hydrogen inlet relative humidity or stoichiometry.

1. Introduction

Fuel cells are considered as environmentally clean and efficient and they could be one of the main electricity generator systems of the future. Even if their governing principles are known for more than 150 years, optimizing fuel cells performances and reliability demands sound understanding of various physical phenomena. Because of this complexity and to the technical difficulties associated with experiments giving access to local data, modelling remains a key point for the improvement of this technology.

Thanks to their low operating temperature and to their high power density, polymer electrolyte membrane fuel cells (PEMFC) are probably the most studied category of fuel cells, especially for transport applications, and significant advances were achieved in the last few years.

In the early 1990s, Bernardi and Verbrugge [1] and Springer et al. [2] developed the first one-dimensional, steady state and isothermal models. These models were not complete but they provided the basis of fuel cells transport modelling by considering phenomena such as water transport in the polymer membrane and gas transport in the gas diffusion layers (GDLs). They also emphasized the importance of water management, the hydration of the membrane being one of the key issue for electrical efficiency [3–5]. On the other hand, it is also well-known that an excess of liquid water could hinder the access of reactive gases to the reaction sites (flooding) [6] and reduce the fuel cell electrical efficiency by decreasing the actual active area. In addition, some authors like Yi and Nguyen [7] or Chen et al. [8] pointed out that water distribution in the cell depends highly on the design of the flow field plates and on the flow configuration (co, cross, or counter flow), which must be considered for an accurate and reliable prediction of fuel cell performances.

Likewise, an accurate modelling of the phenomena occurring in the catalyst layers is required. The first and simplest approach [9] consisting in considering catalyst layers as interfaces between the GDLs and the membrane can lead to an overestimation of the current density and it is probably unsuitable. Nevertheless, a compromise must be achieved between the structural complexity of the active layers and the simplicity and robustness of

* Corresponding author. Tel.: +33 383 595 560; fax: +33 383 595 551.
E-mail address: sophie.didierjean@ensem.inpl-nancy.fr (S. Didierjean).

0378-7753/$ – see front matter © 2010 Elsevier B.V. All rights reserved.
doi:10.1016/j.jpowsour.2010.03.027

Nomenclature

Roman letters

A	fuel cell area (cm^2)
C	concentration ($mol\,m^{-3}$)
D	water diffusion coefficient ($m^2\,s^{-1}$)
e	thickness (μm)
E	voltage (V)
EW	membrane equivalent weight ($g\,mol^{-1}$)
RH	relative humidity
I	current density ($A\,cm^{-2}$)
j_0^C	exchange current density ($A\,m^{-2}$)
k	sorption curves linearized slope
K	absolute permeability of GDL (m^2)
K_H	Henry's constant ($mol\,atm^{-1}\,m^{-3}$)
N	molar flux ($mol\,s^{-1}\,cm^{-2}$)
P	pressure (atm)
R_0	agglomerate radius (μm)
S	saturation
T	temperature (°C)

Greek letters

α_C	charge transfer coefficient
ε	porosity
γ	active layer rugosity
λ	membrane water content
λ_{Air}	air stoichiometry
λ_{H_2}	hydrogen stoichiometry
η	overvoltage (V)
ρ_{dry}	dry membrane density ($g\,m^{-3}$)
ξ	electro-osmotic drag coefficient

Subscripts

A	anode
AC	anodic channel
AE	anodic electrode
C	cathode
CC	cathodic channel
CE	cathodic electrode
CL	catalyst layer
GDL	gas diffusion layer
mem	membrane

Superscript

D	diffusion
EO	electro-osmose
$i/i+1$	number of the discrete element
IN	entrance point of gases

the numerical codes and they are frequently regarded as porous agglomerates composed of catalyst and carbon clusters coated with a thin ionomer layer. Such models are detailed by Sun et al. [10] or Lin et al. [11] and lead to a more detailed description of transport phenomena. In this paper, we present a model developed for control purposes which must be able to compute water and current density distributions whatever the operating conditions. That is the reason why the active layers are considered as interfaces for water transport, i.e., their mass transport resistance is neglected, but the calculation of the concentration overpotentials relies on an agglomerate description.

As far as the geometry is concerned, various kinds of multi-dimensional models have been proposed. In the simplest pseudo-2D approaches, the 1D description of coupled transfer through the cell thickness is complemented by the description of gas depletion and possibly temperature evolutions along the bipolar plate channels [3,4,12]. Other papers describe complete 3D dynamic models [13,14] using Computational Fluid Dynamics (CFD) solvers. However, because of high computation time, CFD codes are not appropriate to be used for the control of fuel cells and for the present work, a pseudo-2D model was preferred. Although results of pseudo-2D model encountered in the literature [15–18] refer to co-flow mode, an interesting aspect of 2D "along the channel" models is the ease with which different flow configurations can be investigated and compared. In our case, we investigate how co- and counter-flow modes affect water distribution and electrical performances. A thermal model is also developed in order to take account of the coupling between temperature, water and current density distributions.

2. Water transport model

2.1. Water transport through the cell thickness

Mass fluxes in fuel cells are complex because many components (water in vapour or liquid phase, oxygen, nitrogen, hydrogen) are present in materials of different structure and functions. In order to focus on the prevailing phenomena, the transport of air and hydrogen through the gas diffusion layers is not taken into account: a preliminary comparison with a multi-component Stefan–Maxwell diffusion model proposed by Ramousse [19] showed that in usual conditions, gas diffusion has no significant impact on water transport. However, the consumption of oxygen and hydrogen along the bipolar plate channels is included in the model. The total pressure is assumed uniform in the whole cell and the electrode mass transport resistances are neglected: they are considered as interfaces between the GDLs and the membrane.

2.1.1. Membrane

2.1.1.1. Diffusive water flux. As reported by Laporta et al. [20], water is liquid in the polymer membrane, which is also assumed impervious to all other fluids. Fick's law is used for estimating the diffusion contribution to the total water flux (in the direction z perpendicular to the membrane plane):

$$N_m^D = -D_m \frac{dC_w}{dz} \tag{1}$$

where D_m is the effective diffusion coefficient of water through the membrane (assumed constant). The membrane water content λ is a non-dimensional concentration defined by:

$$\lambda = \frac{EW}{\rho_{dry}} C_w \tag{2}$$

where EW is the equivalent weight and ρ_{dry} is the density of dry membrane. Denoting λ_{AE} and λ_{CE} the water contents at the anode and cathode sides, respectively, the diffusive water flux is equal to:

$$N_m^D = D_m \frac{\rho_{dry}}{EW} \frac{\lambda_{AE} - \lambda_{CE}}{e_m} \tag{3}$$

This flux is counted positive from the anode to the cathode. λ_{AE} and λ_{CE} depend on the relative humidity of the gas mixtures at the GDL–membrane interfaces according to the sorption isotherms. However, although measuring sorption isotherm is a common practice, very few data are available in the literature and since they were obtained with membranes alone, they must be used with caution in the case of a membrane/electrode assembly (MEA). For this reason and for the sake of simplicity, the sorption curves found in [21,2] at $T = 70$ and 30 °C are approximated by a linear relation (Fig. 1): the slope of the resulting line k is close to 10 and it does not depend on the temperature, thus one can write:

$$\lambda = k.RH \tag{4}$$

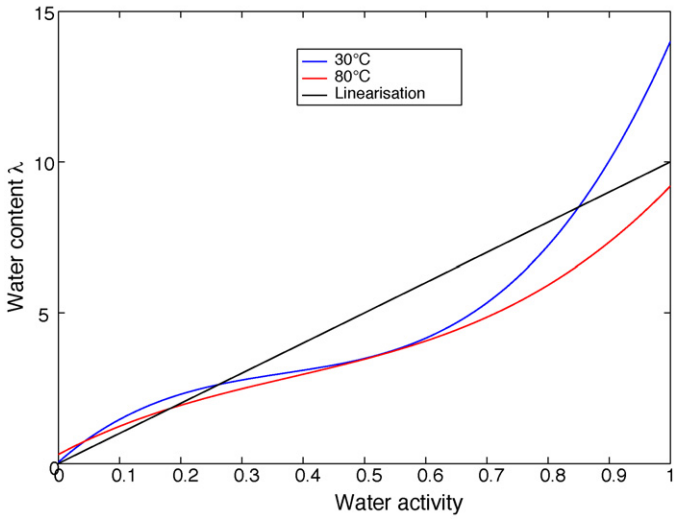

Fig. 1. Linearization of the sorption curves.

When the membrane is immersed in liquid water its water content λ_{liq} is higher than $\lambda_{vap\text{-}sat}$ in a saturated gas at the same temperature T: this phenomenon is referred to as the Schröder paradox [22]. When the membrane–electrode interface is in contact with both liquid water and saturated gas, it is assumed that the resulting water content is equal to [2,23]:

$$\lambda = (1 - S)\lambda_{vap\text{-}sat} + S\lambda_{liq} \tag{5}$$

Usually, the saturation S is defined as the fraction of the pore volume occupied by the liquid phase: $S = V_{liquid}/V_{pore}$; in the case of an interface, S is considered equal to the fraction of the surface in contact with the liquid. According to Weber and Hickner [24], $\lambda_{liq} = 20.4$ at $T = 80\,^{\circ}C$ and Hinatsu et al. [21] gives $\lambda_{liq} = 20.4$ (for Nafion 117) so that $19 \leq \lambda_{liq} \leq 20.4$ between 70 and 80 °C. As a consequence, considering that $\lambda_{liq} - \lambda_{vap\text{-}sat} \approx 10 \approx k$, Eq. (5) becomes:

$$\lambda = k(1 + S) \tag{6}$$

Hence, the diffusive water flux through the membrane can be written as:

$$N_m^D = \frac{X_{AE} - X_{CE}}{R_m} \tag{7}$$

with $R_m = (e_m EW)/(D_m \rho_{dry} k)$ the mass transfer resistance. $X = RH$ for vapour only while $X = S + 1$ in the presence of liquid.

2.1.1.2. Electro-osmotic water flux. The protons drag water molecules when flowing from the anode to the cathode. This electro-osmotic flux is frequently expressed as:

$$N_m^{EO} = \xi \frac{I}{F} \tag{8}$$

The electro-osmotic coefficient ξ stands for the number of water molecules dragged by each moving proton. Among the various expressions of ξ available in the literature (none of them being fully satisfying), the drag coefficient is chosen equal to one [25].

The actual water flux through the membrane is equal to the sum of N_m^D and N_m^{EO}.

2.1.2. Gas diffusion layers

The nature of water fluxes through the GDLs depends strongly on the presence of liquid. In the following, Darcy's law is used to describe the transport of liquid whereas the vapour flux is assumed to be purely diffusive. In practice, two different models are used depending on these two cases; if only a part of the GDL is dry, the location of the interface between the wet and dry zones is treated as an additional unknown.

2.1.2.1. Water transport in vapour phase. If water is in vapour phase at both sides of the GDL, its flux is assumed to be purely diffusive (the convective transport of vapour by the reactant gases passing through the GDLs is neglected) and given by Fick's law:

$$N_m^D = -D_{GDL} \frac{dC_w}{dz} \tag{9}$$

D_{GDL} is the effective diffusion coefficient of vapour through the GDL. It is smaller than the diffusive coefficient of vapour into the bulk gas (air or hydrogen) because in porous media molecules follow longer pathways. To take account of this, the effective diffusion coefficient depends on the porosity and on the tortuosity of the medium. According to the Bruggeman relation for granular packed bed [26], D_{GDL} is given by:

$$D_{GDL} = \varepsilon^{1.5} D_{vapor \to gas} \tag{10}$$

An effective diffusion coefficient in fibrous medium was reported by Pharoah et al. [27] showing that, with a GDL porosity of 0.8, the Bruggeman relation slightly over estimates the diffusion coefficient. This result is consistent with the theory developed by Nam and Kaviany [28].

By considering the vapour as a perfect gas, its concentration in the GDL can be written as:

$$C_W = \frac{RH}{RT} P_{SAT}(T) \tag{11}$$

With RH the relative humidity:

$$RH = \frac{P_{H_2O}}{P_{SAT}(T)} \tag{12}$$

Using Eq. (11) in the Fick's law (9) leads to express the vapour water flow through the GDLs as:

$$N_{GDLvap} = \frac{\Delta RH}{R_{GDL}} \tag{13}$$

with $R_{GDL} = e_{GDL} RT / P_{SAT} D_{GDL}$ the GDL mass transfer resistance and ΔRH the difference in relative humidity between both sides of the GDL. N_{GDLvap} is counted positive from the anode to the cathode.

2.1.2.2. Water transport in liquid phase. Liquid water can appear when vapour reaches its saturation partial pressure. In the GDL, the vapour is supposed to be in equilibrium with the liquid so that the relative humidity is uniform and equal to 1. As a consequence, the vapour diffusive flux is neglected and the mass transfer between the vapour and liquid phases is not considered. Darcy's law is used to describe the liquid water transport through the porous medium:

$$N_{GDLliq} = -\frac{K K_{rl}}{\mu_w} \frac{\rho_w}{M_w} \frac{dP_{liq}}{dz} \tag{14}$$

where K is the permeability of the medium, K_{rl} the relative permeability of the liquid phase, μ_w the water dynamic viscosity and P_{liq} is the pressure of the liquid. ρ_w is the density of water and M_w its molar mass.

According to the definition of the capillary pressure P_{cap} and taking the GDL hydrophobicity into account, $P_{liq} = P_{cap} + P_{gas}$. Pressure losses are neglected and the total gas pressure P_{gas} is constant over the whole cell. Then, it comes:

$$\frac{dP_{liq}}{dz} = \frac{dP_{cap}}{dz} \tag{15}$$

The permeability and the capillary pressure depend on the saturation and the relations between P_{cap}, K_{rl} and the saturation are intrinsic properties of the porous medium. The models of

permeability and capillary pressure used in almost all fuel cell studies rely on empirical correlations established from experimental observations on soil and sand samples. GDL has radically different structures: they are made from carbon fibres and they are treated to be partially hydrophobic so that their transport properties also depend on the spatial distribution of the hydrophobic agent. These properties are difficult to measure because of the small thickness of the samples and of the anisotropy of the materials [29–31]. They can also be estimated by simulation in capillary network models [32].

In this work, the correlations deduced by Kumbur et al. [33] from the experimental results of Gostick et al. [29] are used. For saturations ranging from 0 to 0.8, the capillary pressure measured in commercial GDLs is well correlated by:

$$P_{\text{cap}} = (12.9S + 4.85S^2) \times 10^3 \text{ Pa} \tag{16}$$

Reducing the saturation range to $0 \le S \le 0.6$ makes it possible to use a simpler equation:

$$P_{\text{cap}}(S) = P_0 S^{\alpha_{\text{cap}}} \tag{17}$$

with $P_0 = 10.54 \times 10^3$ and $\alpha_{\text{cap}} = 0.94$.

Combining Eqs. (14)–(16) gives:

$$N_{\text{GDLliq}} = -\frac{KK_{\text{rl}}}{\mu_w}\frac{\rho_w}{M_w}\frac{dP_{\text{cap}}}{dS}\frac{dS}{dz} \tag{18}$$

Kumbur et al. [33] propose the following relation between the relative permeability and the saturation:

$$K_{\text{rl}} = S^{2.16} \tag{19}$$

And introducing (17) and (19) in the flow Eq. (18) leads to:

$$N_{\text{GDLliq}} = -\frac{A_B}{e_{\text{GDL}}}\Delta S^{\alpha_{\text{cap}}+2.16} \tag{20}$$

With $A_B = (\rho_w K/M_w\mu_w)P_0\alpha_{\text{cap}}/(\alpha_{\text{cap}} + 2.16)$. ΔS stands for the difference between the saturations at both ends of the GDL.

Note that since the capillary pressure is continuous in porous media, there is necessarily a saturation step at the interface between two different materials. This is not accounted for between the GDL and the gas channel because of the complexity of the phenomena occurring at this interface (the flows/fluxes are in perpendicular directions).

However, the saturation step at the GDL/electrode interface can be (roughly) estimated. Considering the active layer as a granular porous medium, it is possible to use the equation of Leverett [34] to express the capillary pressure as a function of the saturation, the porosity and the absolute permeability:

$$P_{\text{cap}}(S_{\text{AL}}) = \sigma\cos(\theta)\left(\frac{\varepsilon_{\text{AL}}}{K_{\text{AL}}}\right)^{1/2} J(S_{\text{AL}}) \tag{21}$$

With $J(S) = 1.417S - 2.12S^2 + 1.263S^3$ the Udel's polynomial function [35]. The absolute permeability of the active layer is estimated by the equation of Kozeny–Carman [36,37]:

$$K = \frac{\varepsilon^3 D_{\text{por}}^2}{36kc(1-\varepsilon)^2} \tag{22}$$

with kc the Kozeny–Carman constant, equal to 5, and D_{por} the characteristic dimension of the pores. In the GDL, the capillary pressure is still estimated using the simplified version (17) of the correlation of Kumbur. The structural differences between the GDLs and the active layers are presumably very important but starting from estimates of their main properties given in Table 1, the continuity of the capillary pressure (the equality of Eqs. (17) and (21)) implicates that saturation in the active layer at interface with the GDL is close to zero regardless of the saturation in the GDL. Actually, S_{AL}^0 remains lower that 0.01 even if S_{GDL} reaches one. This result is consistent with those of a recent work by Nam et al. [38]. Consequently, one can reasonably assume that the saturation in the electrode at the interface with the active layer is $S_{\text{AL}}^0 = 0$. However, one must also take into consideration the saturation gradient within the active layer. For the sake of simplicity, let us neglect the source term, i.e., the water flux through the electrode is much lower than the water production, and assume that Eq. (21) is still valid for estimating the capillary pressure, while the relative permeability is given by Corey [39]: $K_{\text{rl}} = S^3$. The equality of the water flux in the GDL (20) and in the active layer yields:

$$\frac{A_B}{e_{\text{GDL}}}S_{\text{CE}}^{\alpha_{\text{cap}}+2.16} = \frac{A_U}{e_{\text{GDL}}}\left(\frac{1.417}{4}S_{\text{AL}}(z)^4 - \frac{4.24}{5}S_{\text{AL}}(z)^5 + \frac{3.789}{6}S_{\text{AL}}(z)^6\right) \tag{23}$$

where

$$A_B = (\rho_w/M_w\mu_w)\sigma\cos(\theta)K_{\text{AL}}(\varepsilon_{\text{AL}}/K_{\text{AL}})^{1/2} \tag{24}$$

and $S_{\text{AL}}(z)$ is the saturation in the active layer as a function of the thickness coordinate z.

Since the water content of the active layer is supposed homogeneous in the transport model (Section 2), one must consider the mean saturation $\langle S_{\text{AL}}\rangle$ in the active layer: in this case, as illustrated in Fig. 2 there is a step between $\langle S_{\text{AL}}\rangle$ and the interface value of S_{GDL}, the mean saturation in the active layer being about 1.5 times higher than at the GDL/active layer interface.

2.1.2.3. Two-zone model. In some cases, the GDLs have to be split into two zones: one where water is in vapour phase only and a second where the transport occurs in liquid phase. An example is depicted in Fig. 3: γ stands for the fraction of the cathode GDL thickness where water flows in liquid phase. At the interface between liquid and vapour zones $RH_\gamma = 1$ and $S_\gamma = 0$. The location of the interface between the two zones (γ) is chosen so that the fluxes are equal in both of them.

Table 1
Estimates of the main structural properties of GDL and electrodes.

	GDL	Electrodes
ε	0.7	0.4
D_{por} (μm)	10	1
K (m^2)	2.12×10^{-12}	3.06×10^{-16}
σ (N m^{-1})	0.0625	0.0625
cos (θ)	0.5	0.5

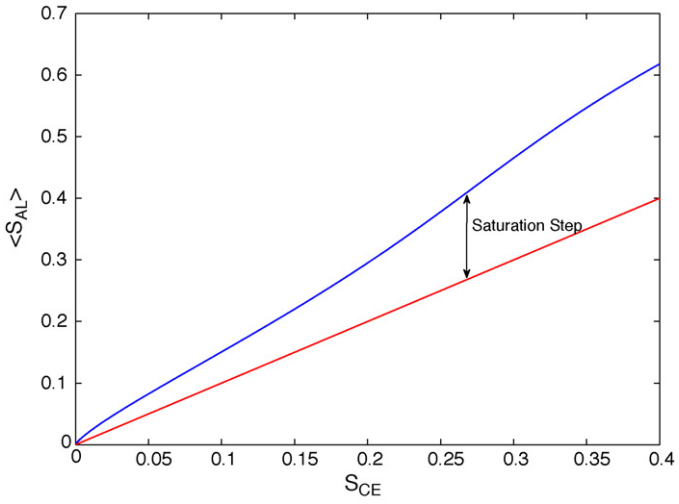

Fig. 2. Step of saturation at the active layer/GDL interface $\varepsilon_{\text{CE}} = 0.7$ and $\varepsilon_{\text{AL}} = 0.3$.

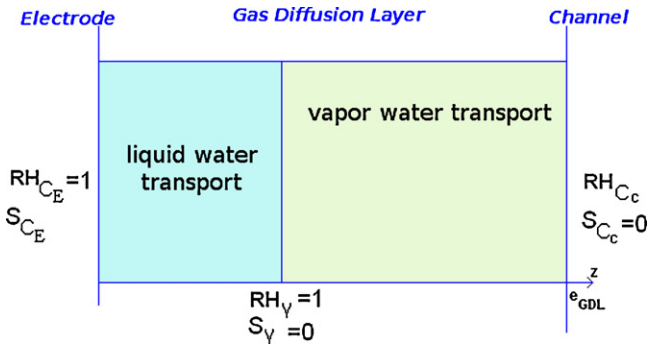

Fig. 3. Partially saturated cathodic gas diffusion layer (GDL).

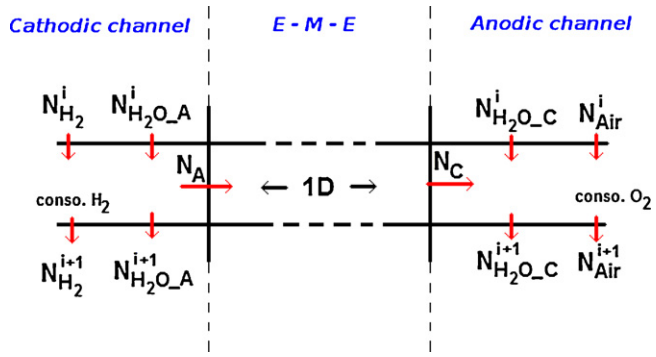

Fig. 5. Pseudo-2D mass balance.

2.1.3. Electrical analogy

In some cases, the 1D equations detailed above for computing water transport from one channel to the other can be represented using an electrical analogy: the potentials or forces are the relative humidities, and the current is the water flux. The equivalent circuit is represented in Fig. 4 where the water flux through the membrane appears as the algebraic sum of a diffusive flux and a constant electro-osmotic flux.

In the absence of liquid and considering the main hypotheses for mass transfer, the governing equations are linear and the electrical analogy is perfectly justified. This is no more the case in the presence of liquid water since the potential is either S (at the GDLs interfaces) or $1+S$ (at the membrane interfaces); furthermore, the equation governing the liquid flow through the GDLs (20) is not linear. However that may be, calculating water fluxes through the thickness of the MEA leads to a system of five equations with five unknowns: three fluxes (in the anode and cathode GDL and in the membrane) and two forces or potentials (at the membrane interfaces). If there is liquid at only one side of the GDL, one more equation and an additional unknown (γ) are necessary and finally, up to seven equations with seven unknowns have to be solved.

There is four key interfaces in the MEA: (1) anode channel/GDL; (2) anode GDL/membrane (the electrode being not considered for water transport); (3) cathode membrane/GDL; (4) cathode GDL/channel. Depending on the state of water at these four interfaces, 16 different cases can be obtained, among which four are not consistent with the conservation of mass (in steady state). Thus, 12 acceptable cases must be considered. The transition between these cases corresponds always to $RH=1$ and $S=0$ at one of the four interfaces.

2.2. Along the channels

2.2.1. Mass balance

The fuel cell is fed by humid air and pure hydrogen. From gas inlet to outlet, the MEA and the gas channels are divided into small volume elements. In each elementary slice, water transport through the GDLs and the membrane is computed using the 1D model. The second dimension corresponds to the flow of water, air and hydrogen along the channels (Fig. 5).

Mass balances in the channel element i allow to compute the gas concentrations, the relative humidity or the liquid saturation used as boundary conditions in the following element (in the direction of the flow):

$$\text{Anode channel}: \begin{cases} N^{i+1}_{H_2O\_A} = N^{i}_{H_2O\_A} - N^{i}_{A} \\ N^{i+1}_{H_2} = N^{i}_{H_2} - \dfrac{1}{N}\dfrac{I}{2F} \end{cases} \tag{25}$$

and

$$\text{Cathode channel}: \begin{cases} N^{i+1}_{H_2O\_C} = N^{i}_{H_2O\_C} + N^{i}_{C} \\ N^{i+1}_{H_2} = N^{i}_{H_2} - \dfrac{1}{N}\dfrac{I}{4F} \end{cases} \tag{26}$$

It is assumed that all gaseous species move at the same velocity in the channels, so that the molar fraction of water is equal to the ratio of the molar flux of water to the total gas flux, which gives this expression for the relative humidity:

$$RH^{i+1} = \frac{P}{P_{SAT}} \frac{N^{i+1}_{H_2Ovap}}{N^{i+1}_{H_2Ovap} + N^{i+1}_{\text{reactant gas}}} \tag{27}$$

The saturation in the gas channel is deduced from the gas and liquid water flow rates by means of the stratified Poiseuille flow theory. Stokes solution gives mass flow ratio of the two fluids

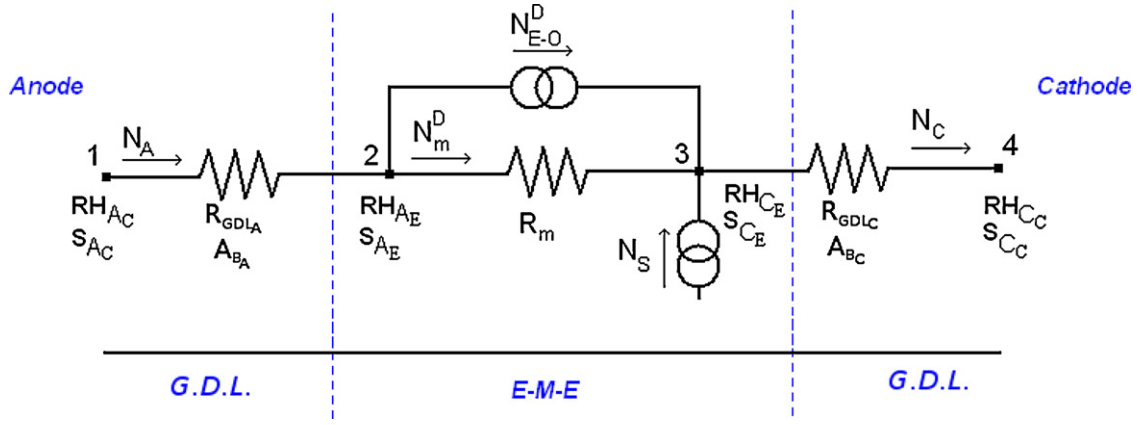

Fig. 4. Electrical equivalent circuit.

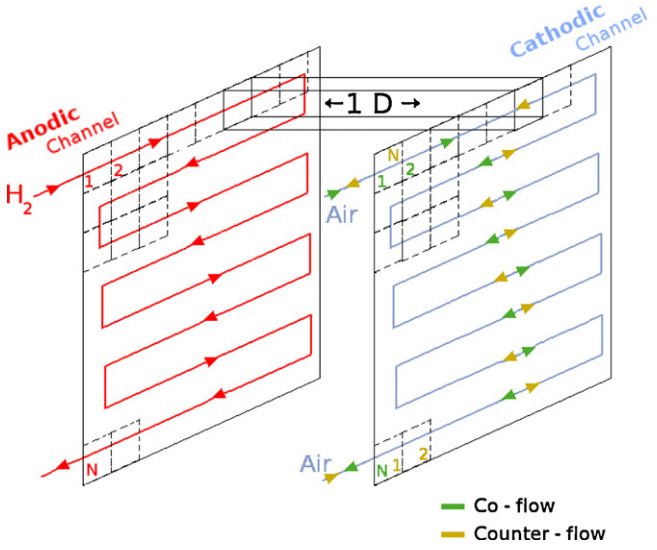

Fig. 6. Co- or counter-flow configurations.

as a function of the ratio of their dynamic viscosities and of the cross-section fractions (from which the saturation is deduced). The temperature dependence of the fluid viscosities is estimated using Sutherland's formula for dry gases and Wilke's formula [40] for gas mixtures. However, water condensation and flow in the gas channels are intrinsically intermittent phenomena and considering them in steady state is only an approximation. The literature describing two-phase flow in channel with a low liquid fraction is scarce [41,42].

2.2.2. Co- and counter-flow

This model allows the investigation of different gas flow configurations.

The bipolar plates at the anode and at the cathode are considered as identical and symmetrical so that the gas channels are parallel as shown in Fig. 6. Thus, hydrogen and air can only flow in the same direction (co-flow configuration) or in opposite directions (counter-flow configuration). Cross-flow configurations are not yet considered in this model.

3. Output voltage

The current density I is computed in each discrete element, the fuel cell output voltage being expressed as:

$$E(T,P) = E_{th}(T,P) - \eta_C - \eta_m \tag{28}$$

where $E_{th}(T,P)$ is the thermodynamic open-circuit voltage. η_C is the potential drop at the cathode and η_m stands for the ohmic loss in the membrane. The potential drop at the anode is neglected compared to that at the cathode.

3.1. Thermodynamic potential

$$H_2 + \tfrac{1}{2}O_2 \leftrightarrow H_2O \tag{29}$$

At constant temperature and pressure, the maximum work that can be produced by a fuel cell is equal to the Gibbs free energy of reaction (25) $\Delta g(T,P_i)$, which yields the following expression for the thermodynamic open-circuit voltage:

$$E_{th}(T,P) = -\frac{\Delta g(T,P_i)}{nF} \tag{30}$$

with $n=2$. Thermodynamics makes it possible to express this voltage as a function of temperature and concentration or partial pressure variations from a standard state (T^0,P^0), which leads to the Nernst equation:

$$E_{th}(T,P) = E^0 - \frac{\Delta s^0}{nF}(T-T^0) - \frac{RT}{nF}\ln\frac{1}{x^0_{H_2}(x^0_{O_2})^{1/2}} - \frac{RT}{nF}\ln\left(\frac{P^0}{P}\right)^{3/2} \tag{31}$$

$x^0_{H_2}$ and $x^0_{O_2}$ are the molar fractions of the reactants at the cell entrance. ΔS^0 is the entropy of the reaction in standard conditions; it is considered as constant in the temperature range of the fuel cell. The thermodynamic voltage in the standard conditions E^0 is equal to 1.23 V.

3.2. Ionic resistance of the membrane

The membrane ohmic drop η_m is given by:

$$\eta_m = R_m I \tag{32}$$

where the ionic resistance of the membrane R_m depends on its local ionic conductivity σ_m. Among the various relations of the literature giving the proton conductivity of membranes as a function of water content and temperature [43], the equation proposed by Zawodzinski et al. [25] is retained. Since the membrane water content is generally non-uniform (Ramousse [19]), its average ionic resistance R_m is obtained by integrating the local values over the membrane thickness:

$$R_m = \int_0^{e_m} \frac{1}{\sigma_m(z)}dz \tag{33}$$

Considering the hypotheses of Section 2.1.1 and in a one-dimensional approach, the water content profile through the membrane can be considered as linear (the electro-osmotic flow does not depend on the water content and the diffusion coefficient is constant and uniform) and it can be deduced from the water content at the interfaces expressed as a function of *RH* and *S*.

Ohmic drops in the other MEA components (electrodes, bipolar plates, backing layers, etc.) and contact resistances are neglected.

3.3. Activation and concentration overpotentials

The electrode overpotentials are well described by the Butler–Volmer equation. The lack of efficiency of PEM fuel cell in terms of electrochemical conversion is mostly due to the oxygen reduction at the cathode. This slow reaction (compared to the hydrogen oxidation) results in a high overpotential η_C and the Butler–Volmer equation can be simplified into the Tafel law [44]:

$$\eta_C = \frac{RT}{\alpha_C nF}\ln\left(\frac{j}{j_0^C}\right) + \frac{RT}{\alpha_C nF}\ln\left(\frac{C^{*0}_{O_2}}{C^0_{O_2}}\right). \tag{34}$$

The exchange current density at the cathode j_0^C depends on the temperature. Starting from the experimental data of Parthasarathy et al. [45], Berning et al. [9] and Ju et al. [46] derived the following equation:

$$j_0^C = \gamma 4.410^{-3}\exp\left(-16456\frac{1}{T} - \frac{1}{353}\right) \tag{35}$$

The roughness factor γ is the ratio of the effective platinum surface (on which the reaction occurs) to the electrode plane area. The actual current density j by reference to the total active surface and the usual current density I (by reference to the MEA plane area) are related by: $I = j\gamma$. $C^{*0}_{O_2}$ is the reference oxygen concentration corresponding to the exchange current density j_0^C [10] and $C^0_{O_2}$ is the

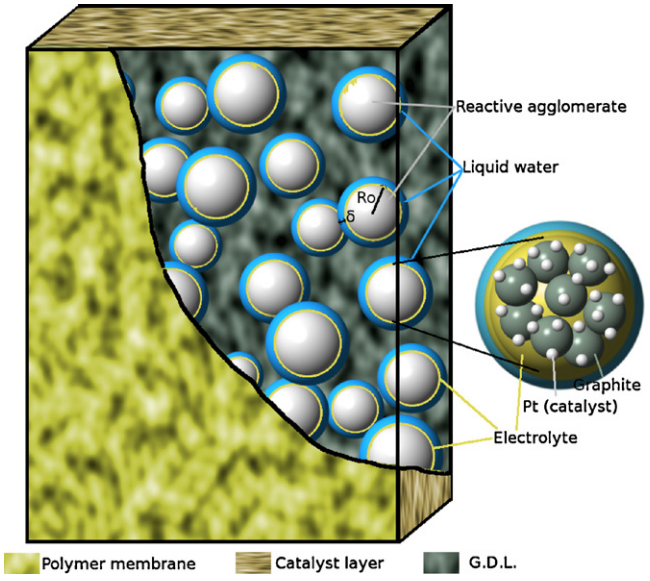

Fig. 7. Agglomerates in the porous electrodes.

oxygen concentration on the active site during fuel cell operation. According to (35), j_0^C increases significantly with the temperature (from 2.32×10^{-2} A m^{-2} at 323 K to 1.76 A m^{-2} at 353 K).

3.3.1. Agglomerate shape and dimension

Understanding the various physical phenomena (ionic, electronic, heat, and mass transfer) taking place at different scales in the catalyst layers is one of the most challenging area of fuel cell modelling. In practice, the geometrical and chemical structure of the catalyst layers depend on the MEA making process and it has a major influence on the actual reaction area. In detailed models, catalyst layers are often considered as porous agglomerates consisting of a homogeneous mixture of carbon, ionomer and platinum or as a mixture of carbon powder and catalyst particles while the electrolyte is assumed to cover only the surface of the pores [10,47–49]. This last representation was retained in the model (Fig. 7).

Two geometrical descriptions of the agglomerates are generally encountered. Madhusudana Rao et al. [50] as well as Lin et al. [11] consider a network of cylinders of length equal to the catalyst layer thickness and of 0.1 μm in diameter. Sun et al. [10] and Jaouen et al. [49] considered spherical agglomerates with a diameter of 1 μm (in some other models, the diameter can be smaller: 0.1 μm in [50,11], 0.5 μm in [51]). Analysing SEM images, Broka and Ekdunge [52] found that the agglomerates characteristic size ranges between 1 and 5 μm while Siegel et al. [53] reported slightly higher values with a mean size of 6 μm. In this work, the agglomerates are considered as spheres of radius R_0 equal to 1 μm (Fig. 7).

3.3.2. Concentration overpotential at the cathode

Water produced by the electro-chemical reaction is assumed to appear at the interface between the carbon and platinum agglomerate and the polymer coating. Moreover, the assumptions described in Section 2.1.2 entail the possible existence of a thin layer of liquid covering the solid phase. The oxygen must diffuse through these two layers before reaching the reaction sites. The oxygen concentration at the reaction point $C^0_{O_2}$ depends on the liquid water layer thickness (δ_w) and on the Nafion layer thickness (δ_n) as well as on the partial pressure P_{O_2} in the pores of the catalyst layer (Fig. 8). The value of the coefficient of diffusion of oxygen in Nafion is not known accurately but considering that the polymer covering the agglomerate is well hydrated by produced water, it should be close to the coefficient of diffusion of oxygen in liquid water $D^{agglo}_{O_2}$. Thus

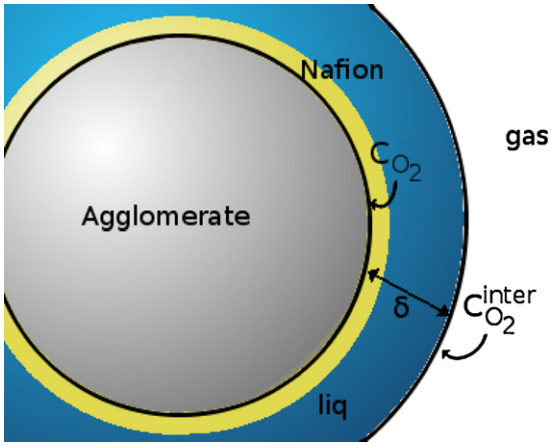

Fig. 8. Liquid layer covering the agglomerate.

numerically, oxygen diffusion occurs through an equivalent layer of thickness $\delta = \delta_n + \delta_w$ and its flux is given by:

$$N_{O_2} = D^{aggl}_{O_2} \frac{C^{inter}_{O_2} - C^0_{O_2}}{\delta} \tag{36}$$

$C^{inter}_{O_2}$ is the concentration of oxygen in equilibrium with the gas phase, given by Henry's law: $C^{inter}_{O_2} = K_H P_{O_2}$ with $K_H(T)$ the Henry constant.

The thicker the liquid layer, the lower the oxygen concentration $C^0_{O_2}$ at the reaction point so that when the maximum thickness δ_{max} is reached $C^0_{O_2} = 0$. Knowing the oxygen flux, δ_{max} is given by:

$$\delta_{max} = \frac{D}{N_{O_2}} C^{inter}_{O_2} \tag{37}$$

And the concentration ratio in the Tafel law (34) becomes:

$$\frac{C^{*0}_{O_2}}{C^0_{O_2}} = \frac{C^{*0}_{O_2}}{x_{O_2} P K_H} \left(\frac{\delta_{max}}{\delta_{max} - \delta} \right) \tag{38}$$

In various studies the thickness of Nafion around the agglomerates δ_n varies between 10 and 100 nm [54,49,10]. Here δ_n is equal to 50 nm. Assuming a uniform distribution of water around the spheres, the thickness of the liquid layer δ_w can be expressed as:

$$\delta_w = R_0 \left(\sqrt[3]{1 + \langle S_{AL} \rangle \frac{\varepsilon_{AL}}{1 - \varepsilon_{AL}}} - 1 \right) \tag{39}$$

ε_{AL} is the porosity of the active layer, R_0 is the radius of the agglomerates and $\langle S_{AL} \rangle$ is related to S_{CE} through Eq. (23).

4. Macroscopic thermal effects

A part of the available hydrogen/oxygen energy is converted into heat. Internal heat production induces local temperature non-uniformity through the cell thickness (Vie and Kjelstrup [55]), which is not considered in the following, and a macroscopic temperature distribution along the gas channels. These temperature profiles have been observed experimentally (Maranzana et al. [56]) and they are highly correlated with the current density and with the appearance of liquid water. Adzakpa et al. [57] presents a 3D thermal modelling of a fuel cell and the temperature evolution along the gas distribution is shown.

Table 2
Default values of the parameters.

	Value	Units	Ref.
Operating conditions			
Cooling temperature ($T^{\text{inlet}}_{\text{cooling}}$)	70	°C	
Pressure (P)	1.6	bar	
Air stoichiometry (λ_{Air})	2	–	
Hydrogen stoichiometry (λ_{H_2})	1.3	–	
Air inlet relative humidity (RH^1_{CC})	0.7	–	
Hydrogen inlet relative humidity (RH^1_{AC})	0.1	–	
Voltage (E)	0.7	V	
Material properties and geometry			
Active area (A)	340	cm^2	
GDL thickness (e_{GDL})	200	μm	
Membrane thickness (e_{men})	20	μm	
GDL porosity (ε_{GDL})	0.8	–	
Catalyst layer porosity (ε_{CL})	0.5	–	
Membrane equivalent weight (EW)	1100	g mol^{-1}	
Dry membrane density (ρ_{dry})	2020×10^3	g m^{-3}	
GDL absolute permeability (K)	2.55×10^{-12}	m^2	[28]
Water diffusion coefficient in the membrane (D_m)	3×10^{-9}	$\text{m}^2\,\text{s}^{-1}$	[28]
Water diffusion coefficient in O_2	3.16×10^{-5}	$\text{m}^2\,\text{s}^{-1}$	[19]
Water diffusion coefficient in H_2	1.61×10^{-4}	$\text{m}^2\,\text{s}^{-1}$	[19]
Physical parameters			
Agglomerate mean radius (R_0)	1	μm	[10]
Thickness of electrolyte film covering each agglomerate (δ_n)	50	nm	
Reference exchange current density, j^c_0 at $T = 70$ °C	2.32×10^{-2}	A m^{-2}	[10]
Reference O_2 concentration, $C^0_{O_2}$ at $T = 70$ °C	0.85	mol m^{-3}	[10]
Cathode transfer coefficient (α_C)	0.4	–	[10]
Catalyst layer roughness (γ)	100	–	
Henry's constant at 25 °C (K_H)	3.2	$\text{mol atm}^{-1}\,\text{m}^{-3}$	
Simplified correlations			
Slope of linearized sorption curves (k)	10	–	
Maximum water content in the membrane, $\lambda_{\text{vap-sat}}$ at $T = 70$ °C	20.4	–	[24]

4.1. Heat sources

The amount of heat produced by the fuel cell Q_{total} is given by:

$$Q_{\text{total}} = \frac{\Delta h}{2F} - E(T,P)I + Q_{\text{H}_2\text{O}} \tag{40}$$

where Δh is the enthalpy of the hydrogen oxidation reaction (29) considering that water is produced in vapour phase. The first term in the right-hand side of (40) depends directly on the fuel cell voltage and current intensity. According to Ramousse et al. [43,58], the second term $Q_{\text{H}_2\text{O}}$ depends on the water fluxes described in Section 2. Strictly speaking, it is related to the phase change of water in the GDLs ($Q^{\text{H}_2\text{O}}_{\text{state change}}$) and also to the sorption/desorption processes at the membrane interfaces. However, the heat of sorption of water being fairly close to its the latent heat of vapourization [19], there is no global heat production linked to the flux of water through the membrane in steady state: sources and sinks at the anode and cathode interfaces compensate each other.

The cell temperature being assumed uniform in the through-plane direction, the sum of the heat sources induced by phase changes of water within the whole MEA and the gas channels is simply given by $Q^{\text{H}_2\text{O}}_{\text{state change}} = L_{\text{vap}} \Delta N^{\text{GDL}}_{\text{H}_2\text{O}}$, where $\Delta N^{\text{GDL}}_{\text{H}_2\text{O}}$ stands for the net amount of liquid flowing out from each volume element.

4.2. Cooling water temperature profile

For the sake of simplicity, the cooling circuit which controls the temperature of the fuel cell is assumed parallel to the gas channels and it is also divided into small volume elements (Fig. 9). The purpose of this work being to investigate the effects of temperature profiles along the gas channel, the temperature of each MEA elementary volume is assumed equal to that of the cooling water. Although the good thermal conductivity of the bipolar plates material justifies partially this hypothesis, it is well known that the temperature is not uniform through the cell thickness [19,55,58] and a more detailed study taking fully into account the coupling between heat, mass and charge transfers will be carried out in the future. As shown in Fig. 9 the cooling circuit is located between two adjacent cells (with identical operating conditions) and the end effects are neglected.

Starting from the local heat production, the rise in cooling water temperature between elements i and $i+1$ is given by a simple heat balance:

$$T^i = T^{i-1} + \frac{Q^i_{\text{total}}}{q_{\text{cooling}} Cp_{\text{cooling}}}, \tag{41}$$

With Cp_{cooling} the water heat capacity and q_{cooling} its mass flow rate. q_{cooling} is chosen so that the difference between the inlet and outlet temperatures is about 5 °C, as observed experimentally in usual conditions (see Table 2). An iterative loop is necessary to take account of the coupling between the temperature, the water flux, and the current density. Water can flow in the same or opposite direction as either of the gases. The fuel cell voltage is constant and homogeneous.

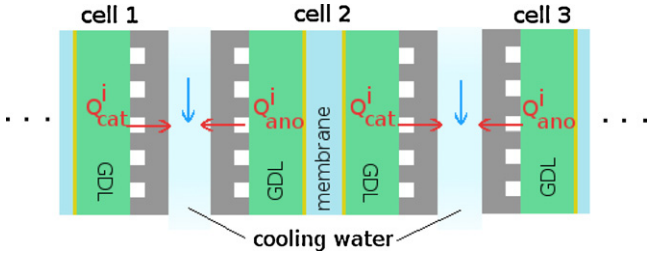

Fig. 9. Cooling water channels between adjacent cells.

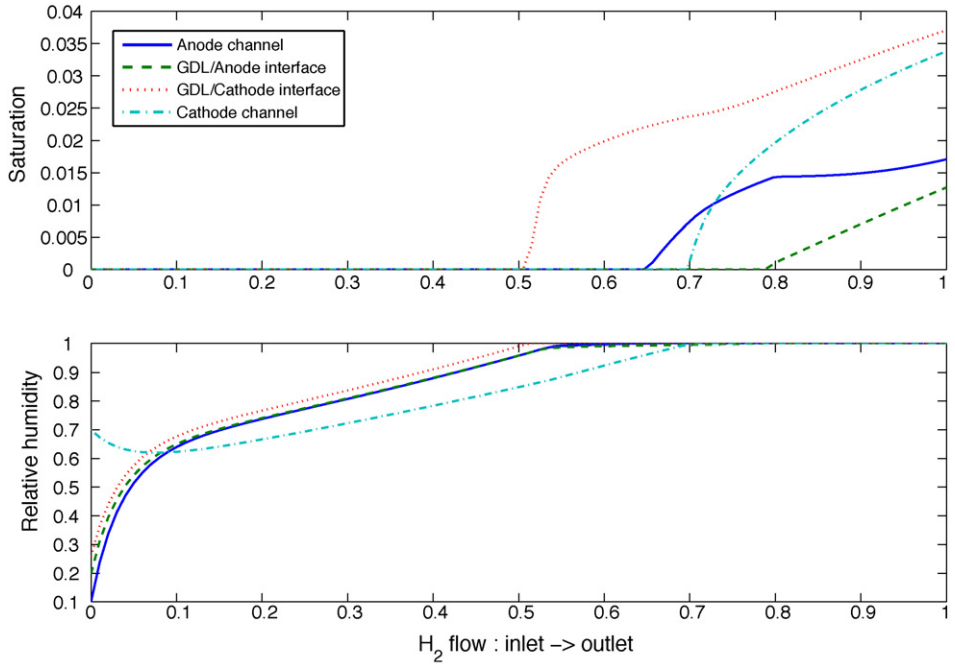

Fig. 10. Water distribution through the cell for default simulation parameters, co-flow configuration, uniform temperature, $E = 0.7$ V, $T = 70\,^{\circ}$C (air and hydrogen inlet in 0).

5. Results

The model makes it possible to investigate the current density, water content, and temperature profiles along the gas channels. In a first part, the temperature is kept constant and next, the effects of its macroscopic variations are discussed.

5.1. Main parameters

The choice of the parameter values is a crucial issue for numerical simulation. In the case of fuel cells, the models need generally a large number of data describing the operating conditions and characterising the materials. Actually, those related to transport phenomena through the porous media of the MEA are rarely well known. This is the case for instance of the water diffusion coefficient in the membrane. In the same way, the constants appearing in Tafel law (34) depend on the catalyst layer making process as well as on the operating conditions. The high sensitivity of the results to such parameters can make them difficult to interpret but it also reflects the significance of some physical phenomena. The list of the parameters and their default value are given in Table 2. Most of the data come from [10,19,28] and [59].

5.2. Current density profiles and water distribution

5.2.1. Uniform temperature in the cell

5.2.1.1. Co-flow simulations at uniform temperature. Hydrogen and air are fed to the fuel cell at the same end with relative humidities RH_{CC}^{IN} and RH_{AC}^{IN} (Table 2) and they flow in the same direction. In order to facilitate the interpretation of the water content and current density profiles in Figs. 10 and 11, the temperature is first kept uniform (70 °C). Fig. 10 depicts the evolution of the water content in terms of relative humidity and saturation at the GDL/electrode interfaces and in the channels. It shows that close to the inlet, the relative humidity decreases in the cathode channel while it rises in the three other points, denoting the existence of a water flux through the cell thickness: the vapour tends to diffuse toward dry hydrogen. Beyond 15% of the total channel length, the water content increases monotonously along the anode and cathode flows and some liquid appears at the cathode/GDL interface near the middle (52%) of the channel. Then, condensation occurs in the anode channel and shortly downstream, in the cathode channel. Once liquid water is present from one channel to the other (beyond 75% of the cell length), the saturations increase slowly so that the maximum values at the exit are lower than 4% (at the electrode/GDL interfaces).

The humidity and saturation profiles are strongly correlated to the current density distribution, as shown in Fig. 11 for two values of the (uniform) temperature: 70 °C in blue (—) and 75 °C in green (- - -). In both cases, the current density rises in the first part of the fuel cell thanks to the increase in membrane hydration and to the decrease of its ionic resistance. However, although the maximum value of the saturation remains under 4%, the current density drops as soon as liquid water appears at the cathode as a consequence of the rise of the concentration overpotential entailed by the diffusion of oxygen through the thin liquid layer covering the agglomerates.

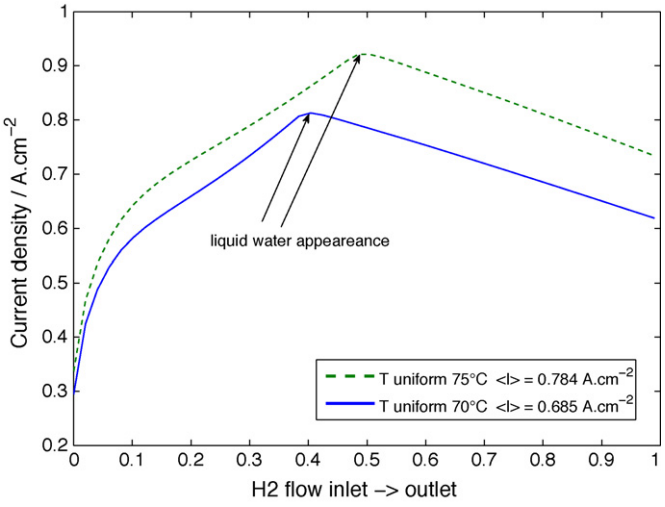

Fig. 11. Current density profile along the cell as a function of (uniform) temperature. Default simulation parameters, co-flow configuration (air and hydrogen inlet in 0), $E = 0.7$ V.

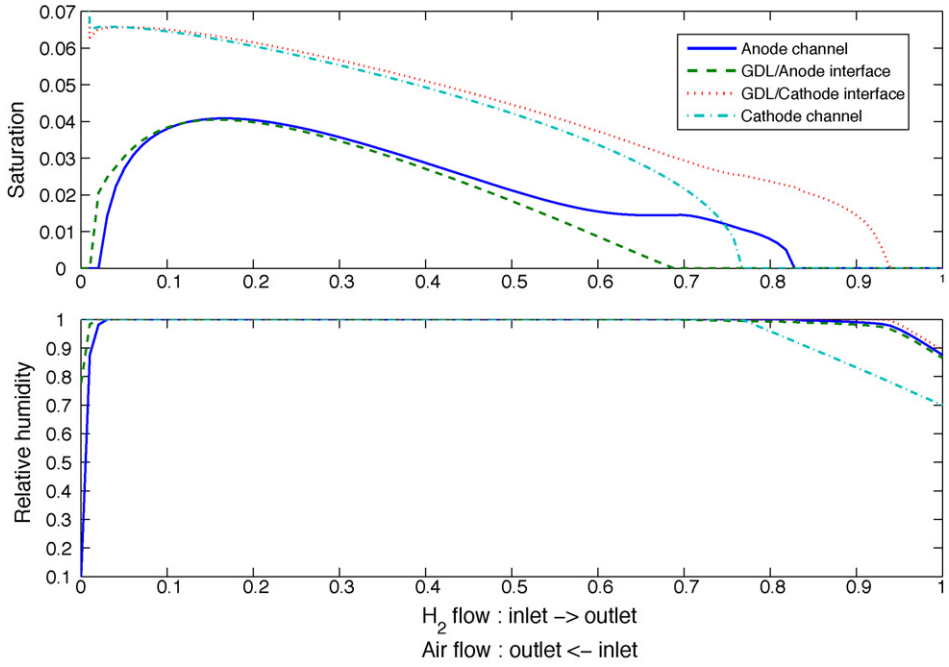

Fig. 12. Water distribution through the cell for default simulation parameters, counter-flow configuration, uniform temperature, $E = 0.7$ V, $T = 70\,^{\circ}$C (hydrogen inlet in 0, air inlet in 1).

Similar tendencies are observed at 75 °C, except that due to the higher saturation pressure, liquid appears further away from the fuel cell inlet. As a consequence, the average relative humidity in the air channel is lower at 75 °C than at 70 °C and the membrane resistance increases from 0.128 to 0.130 $\Omega\,cm^2$ (in spite of the higher temperature). However, the prevailing effect in terms of fuel cell performances is the enhancement of the cathode exchange current density j_0^C (35), which improves the mean current density $\langle I \rangle$ by almost 10%.

Finally, Fig. 11 put forward the large heterogeneity in local current density, which ranges from 0.3 to 0.8 A cm^{-2} at 70 °C. This corresponds to a dispersion of 73% with reference to the mean value (0.68 A cm^{-2}).

5.2.1.2. Counter-flow simulations at uniform temperature. In counter-flow mode, the air and hydrogen inlets are at the opposite ends of the fuel cell. In the following figures, the origin of the horizontal axis corresponds to the hydrogen inlet and air outlet. Fig. 12 depicts the profiles in relative humidity and saturation at the GDL/electrode interfaces and in the channels. By comparison with Fig. 10, the liquid occupies a much larger fraction of the cell and the values of the saturation are higher. Liquid water is always present in the fuel cell cross-section, except near the hydrogen inlet (beyond 95% of the channel length).

The corresponding current density profile is plotted in Fig. 13 (blue (—)). Thank to a better hydration, the membrane ionic resistance is lower in counter-flow than in co-flow (0.092 $\Omega\,cm^2$ instead of 0.128 $\Omega\,cm^2$) and the average current density is about 8 to 10% higher. The increase in concentration overpotential induced by the presence of liquid at the cathode has a low impact. Fig. 13 also points out a steady increase in current density along the hydrogen channel, except for the small zone near the outlet where liquid disappears and where the membrane ionic resistance increases because of a large water flux through the membrane toward the unsaturated air. Finally, the local current density ranges from 0.55 to 0.87 A cm^{-2}, which corresponds to a dispersion of 42% with reference to the mean value (0.74 A cm^{-2}). This is significantly lower than the dispersion observed in co-flow.

As expected, the average current density is higher at 75 °C than at 70 °C and this time, it begins to decrease slightly sooner at 75 °C as the liquid disappears. One again, the prevailing phenomenon in terms of fuel cell performance is the enhancement of the cathode exchange current density j_0^C (35): the improvement of the average current density reaches about 17% by reference to the value obtained at 70 °C. The effect of temperature is higher than in co-flow because of the small impact of the saturation pressure on membrane hydration, the fuel cell being hydrated mostly by liquid water.

5.2.2. Influence of the macroscopic temperature profile

In this section, two cases are considered depending on the direction of the flow of cooling water by reference to hydrogen: co-flow

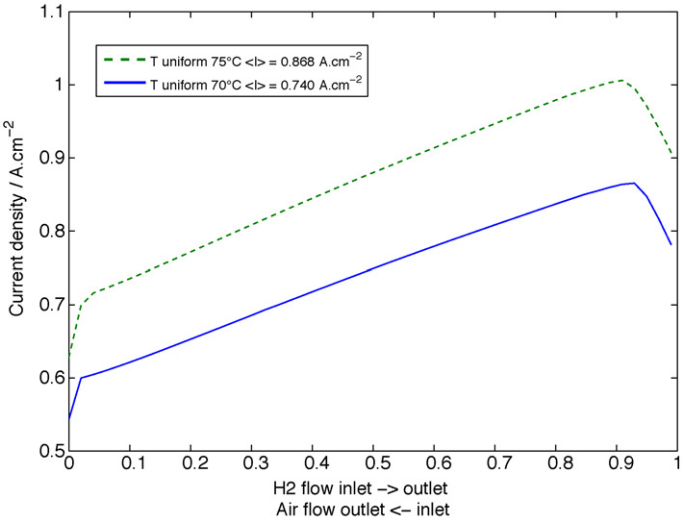

Fig. 13. Current density profile along the cell as a function of (uniform) temperature. Default simulation parameters, counter-flow mode (hydrogen inlet in 0), air inlet in 1, $E = 0.7$ V.

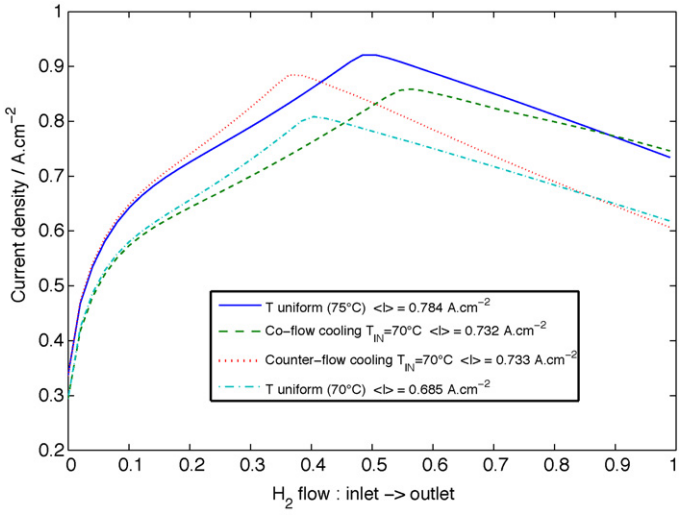

Fig. 14. Current density profiles along the cell as functions of the direction of the flow of cooling water. Co-flow configuration for gases, default parameters, $E = 0.7$ V.

cooling (- - -) or counter-flow cooling (···). As mentioned earlier (Section 4.2), the water flow rate is adjusted so that its temperature rises from 70 °C at the inlet to 75 °C at the outlet. Figs. 14 and 15 depict the corresponding current density and temperature profiles. For comparison, those obtained with uniform temperatures (70 °C (-·-·-·) and 75 °C (—)) and discussed in Section 5.2.1 are also plotted in Fig. 14. In Figs. 14 and 15, air and hydrogen flow in the same direction but the values of the electric power obtained in the co-flow configuration are reported in Table 3.

It appears clearly from the results of Table 3 and of Fig. 14 that the fuel cell performances depend mostly on the mean value of the temperature, which confirm that over this range of operating conditions, the prevailing parameter is the cathode exchange current density j_0^C (35). On the other hand, the comparison between the green (- - -) and red (···) curves in Figs. 14 and 15 put forward some qualitative effects of the direction of the flow of cooling water: for instance, counter-flow cooling lowers the fuel cell temperature and thus promotes water condensation close to the gas channel exits. It also improves the current density close to the gas inlets. On the contrary, co-flow cooling delays the appearance of liquid water close to the gas exits but reduces the current density near the gas inlets.

Table 3
Fuel cell electric power as a function of temperature and of the direction of gases and cooling water. Other parameters are given in Table 2.

Temperature model	Gas flow configuration	
	Co-flow	Counter-flow
$T_{uniform} = 70$ °C	163.0 W	176.4 W
$T_{uniform} = 75$ °C	186.6 W	206.3 W
Cooling water flow in the same direction as H_2, $T^{IN} = 70$ °C	174.2 W	187.1 W
Cooling flow in the opposite direction as H_2, $T^{IN} = 70$ °C	174.4 W	187.8 W

Fig. 15 shows that the slope of the temperature profiles are linked to the variations in current density. The lowest slope (i.e., the lowest heat flux from the fuel cell to the cooling water) corresponds to the highest local current density. The cell mean temperature does not show any significant changes ($\langle T \rangle = 72.48$ °C with a cooling in co-flow and $\langle T \rangle = 72.38$ °C in counter-flow).

In order to highlight the effect of the temperature on the membrane hydration, the operating conditions are modified so that gases are introduced with a very low humidity (2% *RH* for hydrogen and 10% *RH* for air). Then the gases and cooling water inlet temperature is set either to 40 °C (◯) or 70 °C (◊). The corresponding current density profiles are plotted in Fig. 16 (air, hydrogen, and the cooling water flow in the same direction).

In the previous cases, the cathode exchange current density j_0^C was governing the results and the current densities were always better at the highest temperatures. Fig. 16 shows that when the humidification of gases is low, the membrane hydration becomes the limiting phenomena so that over a large fraction of the channel length (between 0 and 45%), the current density is equal or higher at low temperature (◯) than at high temperature (◊): due to the lowest vapour saturation pressure at 40 °C (0.073 bar instead of 0.3 bar at 70 °C) the production of water by the fuel cell leads to a significant increase of the relative humidity of the gases, of the membrane hydration, and of its ionic conductivity. Close to the fuel cell inlet, the lower membrane resistance at 40 °C prevails over the higher exchange current density at 70 °C. On the other hand, Fig. 16 also shows that flooding of the electrodes appears early at 40 °C (starting from 25% of the total channel length), which results in a stagnation of the current density downstream whereas it rises steadily along the channel at 70 °C.

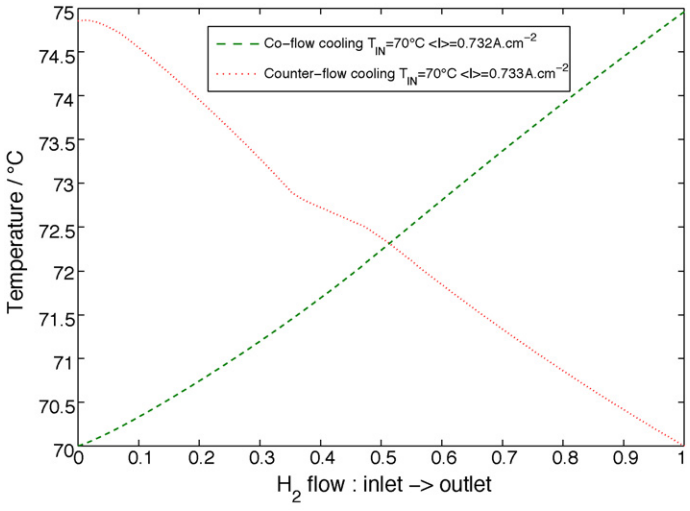

Fig. 15. Temperature profiles along the cell as functions of the direction of the flow of cooling water. Co-flow configuration for gases, default parameters, $E = 0.7$ V. $\langle T \rangle = 72.48$ °C with co-flow cooling and $\langle T \rangle = 72.38$ °C with counter-flow cooling.

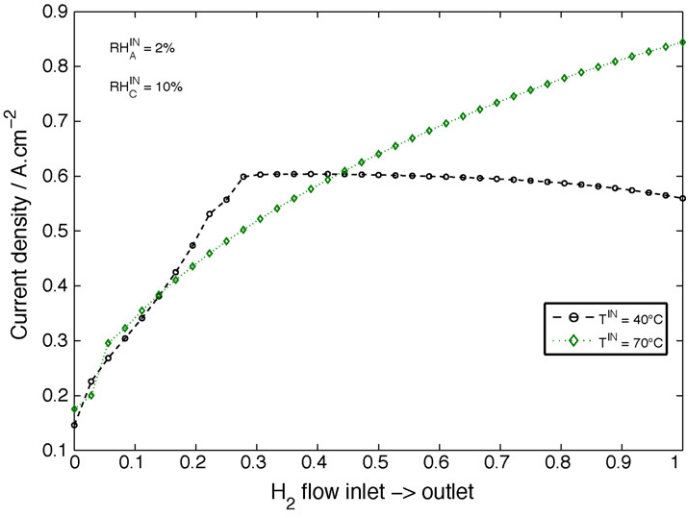

Fig. 16. Impact of temperature on current distributions in dry conditions. The gases and the cooling water flow in the same direction. $E = 0.6$ V. The cooling water flow rate is adjusted so that its temperature rises by 5 °C between inlet and outlet.

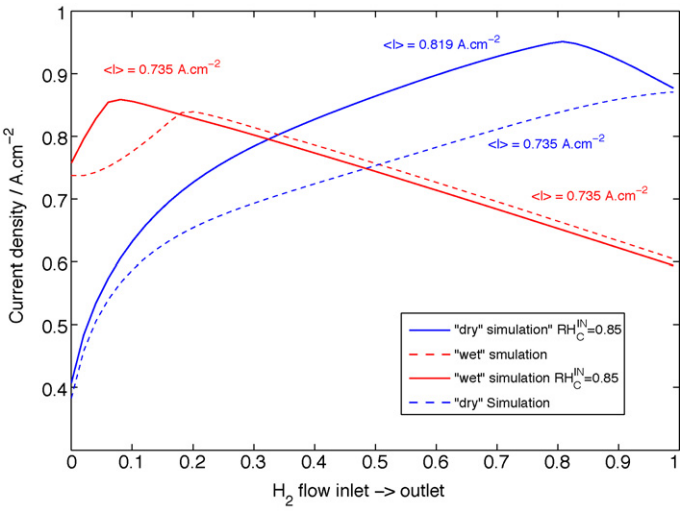

Fig. 17. Current density profiles with different operating conditions. Plain lines: default parameters except that in the "wet" case, the inlet *RH* of hydrogen is set to 85% while in the "dry" case, the inlet temperature is increased to 80 °C and the hydrogen stoichiometry is set to 3. Dotted lines: same conditions but the air *RH* is increased to 85%. $E = 0.6$ V. The cooling water flow rate is adjusted so that its temperature rises by 5 °C between inlet and outlet.

Since the membrane hydration, the electrodes flooding and the exchange current density can have antagonist effects on the cell performance, different sets of operating parameter can lead to the same values of voltage and current intensity. This is illustrated in Fig. 17 by the comparison of the current density profiles obtained by modifying a few of them starting from the default values of Table 2. In the "wet" case, the inlet relative humidity of hydrogen is set to 85% while in the "dry" case, the (gases and cooling water) inlet temperature is increased to 80 °C and the hydrogen stoichiometry is set to 3. In both cases, the average current density is equal to 0.735 A cm^{-2}, in spite of the difference in the profiles. However, the fuel cells response to a change in one of the common parameters can be different: for instance, if the air inlet relative humidity is increased from 70% to 85%, the current density remains equal to 0.735 A cm^{-2} when liquid water is already present in the cell while it rises up to 0.819 A cm^{-2} in the other case. Indeed, since the channels are initially dry, the membrane resistance decreases from 0.144 to 0.133 Ω cm^2 (Fig. 17). These results show that the knowledge of the local current densities can be useful to understand and to predict the behavior of the fuel cell.

5.3. Fuel cell performance and water management

Included in this section is a discussion of the fuel cell global performance (in terms of voltage and mean current intensity) dependence on the operating parameters. Some results about the water transport coefficient are also presented. The water transport coefficient $\alpha - \alpha_0$ is defined as the net water flux through the membrane divided by the water production. α denotes the ratio between the outlet anode water flux and the water production while α_0 is the ratio of water fed to the fuel cell with hydrogen to the water production. For simplicity, the fuel cell is assumed isothermal and the default values of the parameters are those given in Table 2.

5.3.1. Fuel cell performance and water transport coefficient in standard conditions

Fig. 18 (left) shows the fuel cell voltage and electric power as a function of the mean current density and of the gas flow configuration. The curves are similar in shape in both cases but the performance is always better in counter-flow mode. The difference is weak at low current density, showing that the gas flow config-

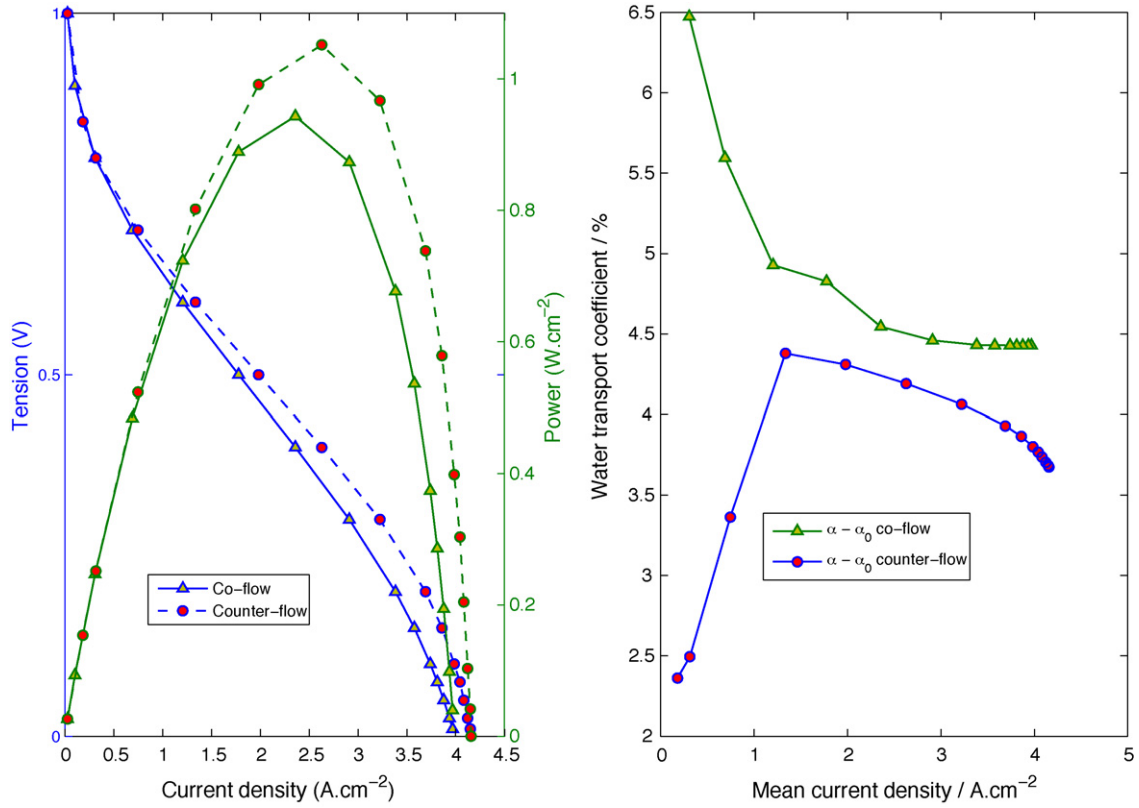

Fig. 18. Voltage and electric power (left) and water transport coefficient (right) vs. mean current density in co-flow and counter-flow mode. Uniform temperature, $T = 70$ °C.

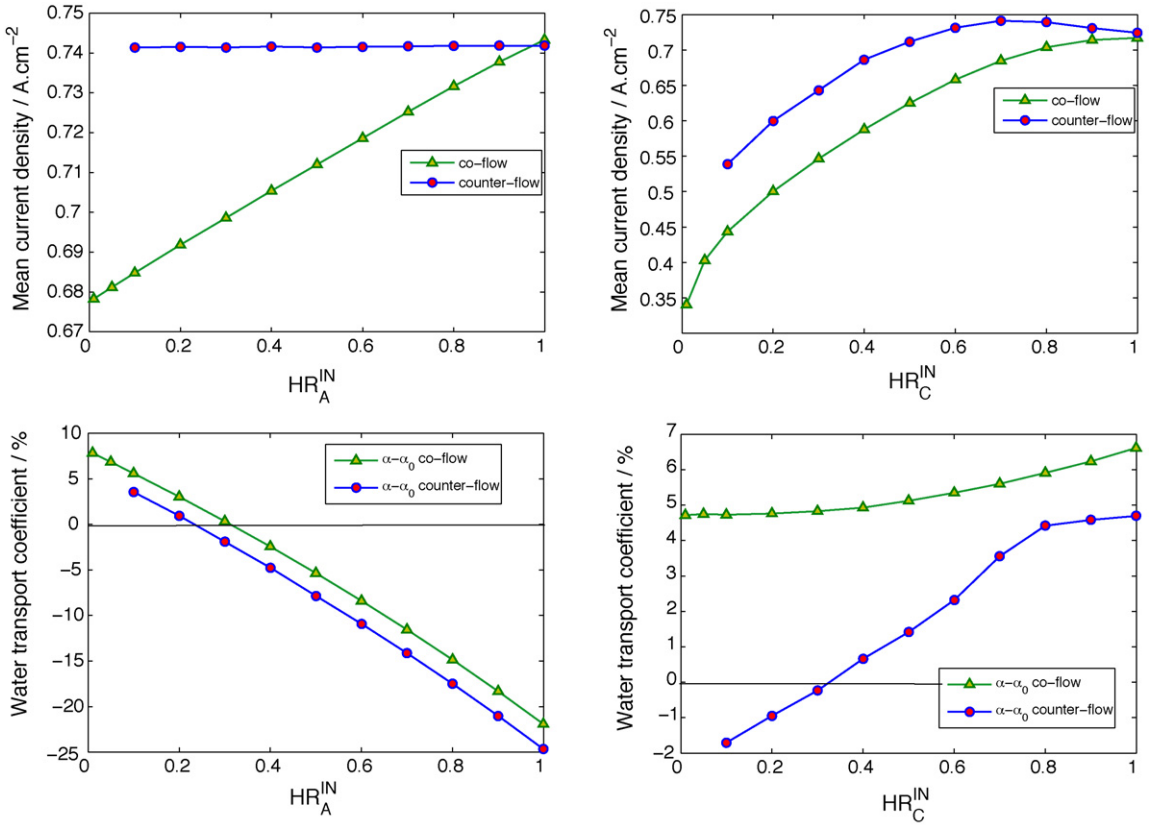

Fig. 19. Water transport coefficient and mean current density dependence on the relative humidity of hydrogen (left, with $RH_C^{IN} = 70\%$) and air (right, with $RH_A^{IN} = 10\%$) in co- and counter-flow. Constant voltage, $U = 0.7$ V, and uniform temperature, $T = 70\,^{\circ}$C.

uration has no significant impact on the activation losses, but it increases with the current density as an effect of the better membrane hydration. Note that the difference between the maximum power estimated in co-flow and in counter-flow reaches 11% (by reference to the lowest value).

It appears in Fig. 18 (right) that the net water transport coefficient remains positive whatever the current density but its values are low in spite of the difference between the air and hydrogen inlet relative humidity (70% and 10%, respectively). However, the plots of the water transport coefficient $\alpha - \alpha_0$ vs. the mean current density show a strong difference in behavior: it increases in counter-flow but decreases in co-flow. In both cases, the values seem to converge to about 4.5% for current densities above 1.5 A cm^2. The water transport coefficient is always lower in counter-flow.

5.3.2. Fuel cell performance and water transport coefficient as functions of the operating conditions

In the following, the fuel cell voltage is kept constant ($E = 0.7$ V).

5.3.2.1. Humidity of air and hydrogen. Fig. 19 shows the variations of the water transport coefficient and of the current density as functions of the hydrogen (left) and air (right) inlet relative humidity. The effect of the hydrogen relative humidity does not depend on the flow direction of the gases: in each case, the water transport coefficient $\alpha - \alpha_0$ decreases (until −25%) as the hydrogen *RH* increases (Fig. 19, top left), which means that the water flow rate at the anode outlet can be lower than at the inlet.

In standard conditions ($RH_A^{IN} = 10\%$ and $RH_C^{IN} = 70\%$, the membrane mean ionic resistance is 0.135 Ω cm^2 in co-flow instead of only 0.089 Ω cm^2 in counter-flow because of a less homogeneous hydration. As a consequence, the mean current density improves (by about 5%) when the hydrogen inlet *RH* increases from 10% to 100% (Fig. 19, bottom left). The membrane ionic resistance reaches 0.108 Ω cm^2 when the hydrogen inlet *RH* is equal to 90%. On the contrary, in counter-flow, both the membrane ionic resistance and the current density remain constant as the hydrogen inlet *RH* increases.

In co-flow, the water transport coefficient is only slightly sensitive to the air inlet relative humidity (Fig. 19, top right), its value rising from 4% to 7%. In counter-flow, its variations are slightly more important but they remain lower than 7 percentage points over the entire range of air inlet *RH*. However, one can note that $\alpha - \alpha_0$ is negative when the incoming air is dry and positive when it is well humidified. An increase of the water transport coefficient with the air inlet relative humidity has been also observed experimentally by Colinart et al. [60].

In co-flow and counter-flow, the current density increases significantly with the air inlet relative humidity (Fig. 19, bottom right). In counter-flow, a maximum can be observed close to $RH_C^{IN} = 70\%$, beyond which the fuel cell performance decreases slightly because of the accumulation of liquid water on the electrodes and in the gas diffusion layers, as shown by the subsequent increase of the cathode overpotential. The membrane ionic resistance is also very sensitive to the humidification of air: in co-flow, it decreases from 0.380 to 0.128 Ω cm^2 when RH_C^{IN} increases from 20% to 70%; in counter-flow the same behavior is observed, but with only a slight reduction beyond $RH_C^{IN} = 70\%$ ($R_{mem} = 0.092\ \Omega\ cm^2$ for $RH_C^{IN} = 70\%$ and $R_{mem} = 0.088\ \Omega\ cm^2$ for $RH_C^{IN} = 100\%$).

5.3.2.2. Stoichiometry of air and hydrogen. Fig. 20 shows the variations of the water transport coefficient and of the current density as functions of the stoichiometry of hydrogen (left) and air (right).

The effects of the hydrogen stoichiometry on the water transport coefficient do not depend on the flow direction of the gases: in

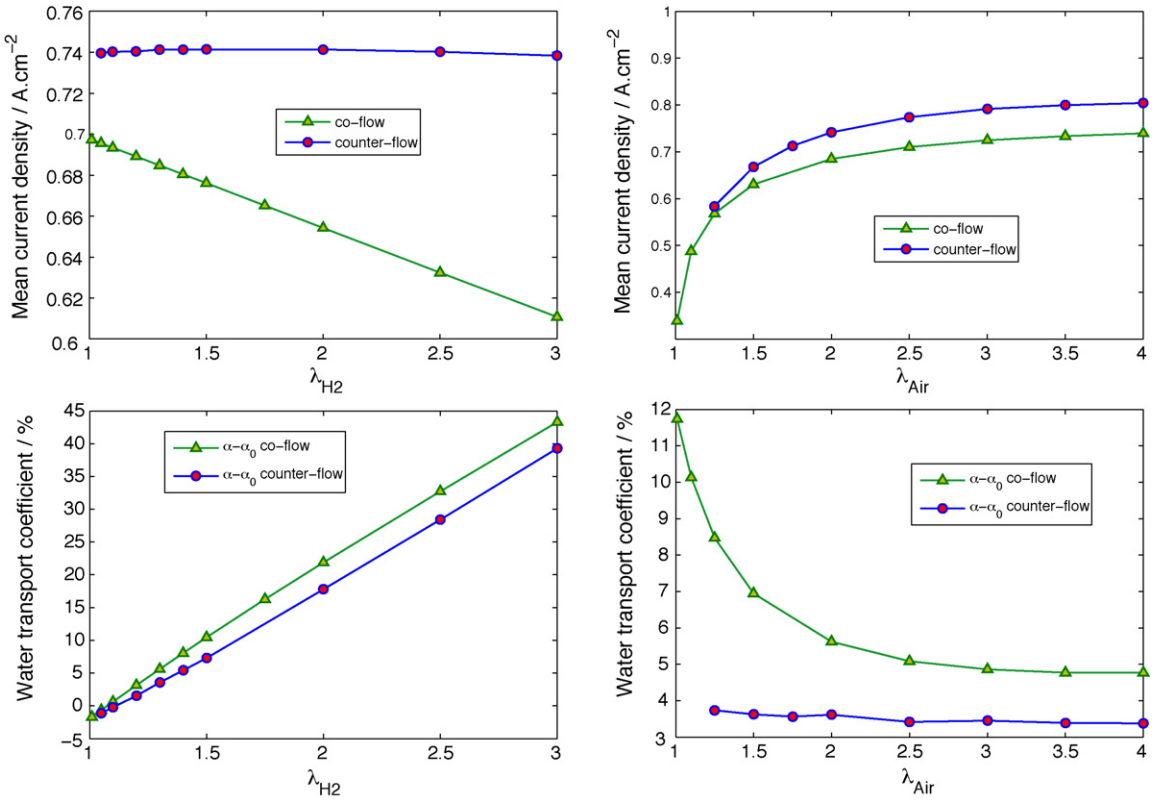

Fig. 20. Water transport coefficient and current density vs. the stoichiometry of hydrogen (left, with $\lambda_{Air} = 2$) and air (right, with $\lambda_{H_2} = 1.3$) in co- and counter-flow. Uniform voltage $U = 0.7$ V and uniform temperature $T = 70\,^{\circ}$C.

each case, $\alpha - \alpha_0$ rises significantly (up to 40 percentage points) and almost linearly with λ_{H_2} (Fig. 20, top left). These results are consistent with those of Büchi and Srinivasan [61]. As far as the current density is concerned, the results depend on the flow direction of the gases. In co-flow, the current density decreases significantly with λ_{H_2} as a results of an increase of the membrane ionic resistance in the presence of dry hydrogen ($R_{mem} = 0.128\,\Omega\,cm^2$ for $\lambda_{H_2} = 1.3$ and $R_{mem} = 0.173\,\Omega\,cm^2$ for $\lambda_{H_2} = 3$). In counter-flow, the current density shows no variations with λ_{H_2} because of the better hydration of the membrane (Fig. 20, bottom left): the macroscopic state of the cell remains unchanged as the hydrogen stoichiometry varies.

When the air stoichiometry increases from 1.1 to 4 (Fig. 20, top right) the water transport coefficient $\alpha - \alpha_0$ decreases very slightly in counter-flow. In co-flow however, it drops by more than 7 percentage points and its value seems to tend toward about 5%. When the air flow and thus the air stoichiometry are low, the saturation and the relative humidity in the air channel becomes rapidly high close to the inlet. In co-flow this leads to an important water flux through the membrane toward dry hydrogen but in counter flow, this water flux is blocked by the saturation of the hydrogen flow near the exit and $\alpha - \alpha_0$ remains constant whatever the air stoichiometry. This result is consistent with the experimental observations of Colinart et al. [60].

The effects of the air stoichiometry on the mean current density are qualitatively identical in co- and counter-flow (Fig. 20), bottom right, with an important increase followed by the stabilization of the values above $\lambda_{Air} = 3$: this is due mostly to the oxygen starvation at low air stoichiometry (in co-flow for instance, the mean oxygen molar fraction in the catalyst layer is 9.7% for $\lambda_{Air} = 1.2$ and 15.9% for $\lambda_{Air} = 4$).

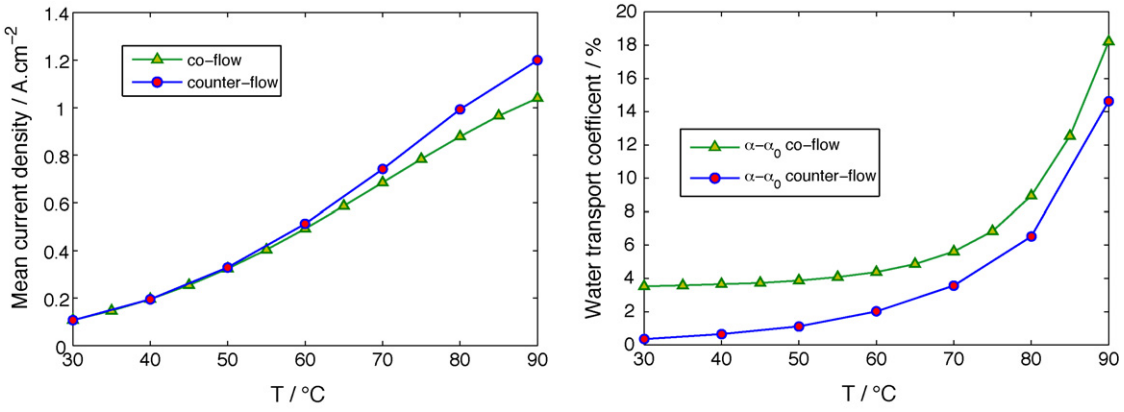

Fig. 21. Water transport coefficient and mean current densities vs. temperature. Co- and counter-flow modes. $U = 0.7$ V.

5.3.2.3. Temperature. The variations of the water transport coefficient and of the current density with the temperature are plotted in Fig. 21. The results do not depend significantly on the flow direction of air and hydrogen. The water transport coefficient shows only a small dependence on the temperature below 70 °C but it increases more steeply at higher temperatures: in co-flow, $\alpha - \alpha_0 = 3.7\%$ at 30 °C, $\alpha - \alpha_0 = 4.8\%$ at 70 °C and $\alpha - \alpha_0 = 18\%$ at 90 °C. The current density is very sensitive to the temperature: in counter-flow, it reaches only 0.1 A cm^{-2} at 30 °C and 1.2 A cm^{-2} at 90 °C. The results depend on the direction of the flow of the gases only above 60 °C with, as expected, higher values in counter-flow because of the better hydration of the membrane.

6. Conclusion

In this paper, we report results of a polymer membrane fuel cell model which was developed for control purposes with the objective to compute rapidly water and current density distributions whatever the operating conditions. Therefore, a compromise had to be achieved between the structural complexity of the membrane, gas diffusion and active layers, the complexity of the two-phase flows, and the simplicity and robustness of the numerical code. That is the reason why a pseudo-2D approach was chosen. A special emphasis was laid on the analysis of the two-phase flow in the gas diffusion layers and of its link with the saturation at the electrode. The impact of the presence of liquid and vapour on the fuel cell performance was thoroughly depicted. The model also allows to simulate and to compare different flow configurations regarding gases (hydrogen and air can flow in the same or opposite direction) and the cooling water.

The flow direction of cooling water does not seem to have significant effect in terms of fuel cell global performance, although it modifies the current density distribution along the cell. The prevailing parameter is the mean temperature, not the temperature profile.

On the other hand, the direction of air and hydrogen can modify greatly the fuel cell mean current density and the net water transport coefficient. In all of the tested cases, the counter-flow mode was preferable. Furthermore, it results in constant performance regardless of the hydrogen inlet relative humidity or stoichiometry thanks to a more homogeneous membrane hydration.

Of course, the flow of gases in actual fuel cells do no correspond necessarily to either co- or counter-flow modes but the model confirms that an optimized design of the flow field channels should result in a more stable operation.

References

[1] D.M. Bernardi, M.W. Verbrugge, AIChE J. 37 (8) (1990) 1151–1163.
[2] T.E. Springer, T.A. Zawodzinski, S. Gottesfeld, J. Electrochem. Soc. 138 (8) (1991) 2334–2342.
[3] T.V. Nguyen, R.E. White, J. Electrochem. Soc. 140 (8) (1993) 2178–2186.
[4] T.F. Fuller, J. Newman, J. Electrochem. Soc. 140 (5) (1993) 1218–1225.
[5] T. Okada, G. Xie, M. Meeg, Electrochim. Acta 43 (14–15) (1998) 2141–2155.
[6] H. Li, Y. Tang, Z. Wang, Z. Shi, S. Wu, D. Song, J. Zhang, K. Fatih, J. Zhang, H. Wang, Z. Liu, R. Abouatallah, A. Mazza, J. Power Sources 178 (2007) 103–117.
[7] J.S. Yi, T.V. Nguyen, J. Electrochem. Soc. 145 (4) (1998) 1149–1159.
[8] F. Chen, Y. Wen, H. Chu, W. Yan, C. Soon, J. Power Sources 128 (2004) 125–134.
[9] T. Berning, D.M. Lu, N. Djilali, J. Power Sources 106 (1–2) (2002) 284–294.
[10] W. Sun, B. Peppley, K. Karan, Electrochim. Acta 50 (16–17) (2005) 3359–3374.
[11] G. Lin, W. He, T.V. Nguyen, J. Electrochem. Soc. 151 (12) (2004) 1999–2006.
[12] O. Lottin, B. Antoine, T. Colinart, S. Didierjean, G. Maranzana, C. Moyne, J. Ramousse, Int. J. Therm. Sci. 1–48 (2009) 133–145.
[13] Z.H. Wang, C.Y. Wang, K.S. Chen, J. Power Sources 94 (2001) 40–50.
[14] S. Shimpalee, S. Greenway, D. Spuckler, J.W. Van Zee, J. Power Sources 135 (2004) 79–87.
[15] O. Lottin, B. Antoine, T. Colinart, S. Didierjean, G. Maranzana, C. Moyne, J. Ramousse, Int. J. Therm. Sci. 1 (2009) 133–145.
[16] D. Singh, D.M. Lu, N. Djilali, Int. J. Eng. Sci. 37 (4) (1999) 431–452.
[17] W. He, J.S. Yi, T.V. Nguyen, AIChE J. 46 (10) (2000) 2053–2064.
[18] K.P. Adzakpa, K. Agbossou, Y. Dube, M. Dostie, M. Fournier, A. Poulin, Energy Convers. 23 (2) (2008) 581–591.
[19] J. Ramousse, PhD Thesis, LEMTA-INPL, 2005.
[20] M. Laporta, M. Pegoraro, L. Zanderighi, Phys. Chem. Chem. Phys. 1 (1999) 4619–4628.
[21] J.T. Hinatsu, M. Mizuhata, H. Takenaka, J. Electrochem. Soc. 141 (6) (1994) 1493–1498.
[22] P. Schroeder, Z. Phys. Chem. 45 (1903) 57.
[23] A.Z. Weber, J. Newman, J. Electrochem. Soc. 153 (12) (2006) 2205–2214.
[24] A.Z. Weber, M.A. Hickner, Electrochim. Acta 53 (2008) 7668–7674.
[25] T.A. Zawodzinski, J. Davey, J. Valero, S. Gottesfeld, Electrochim. Acta 40–3 (1995) 297–302.
[26] A. Souto, PhD Thesis, LEMTA-INPL, 1993.
[27] J.G. Pharoah, K. Karana, W. Sun, J. Power Sources 161 (1) (2006) 214–224.
[28] J.H. Nam, M. Kaviany, Int. J. Heat Mass Transf. 46 (2003) 4595–4611.
[29] J.T. Gostick, M.W. Fowler, M.A. Ioannidis, M.D. Pritzker, Y.M. Volfkovich, A. Sakars, J. Power Sources 156 (1) (2006) 375–387.
[30] E. Arato, M. Pinna, P. Costa, J. Power Sources 158 (1) (2006) 200–212.
[31] Q. Ye, T.V. Nguyen, J. Electrochem. Soc. 154 (12) (2007) 1242–1251.
[32] B. Markicevic, A. Bazylak, N. Djilali, J. Power Sources 171 (2) (2007) 706–717.
[33] E.C. Kumbur, K.V. Sharp, M.M. Mench, J. Power Sources 168 (2) (2007) 356–368.
[34] M.C. Leverett, Trans. AIME 142 (1941) 341–358.
[35] K.S. Udell, Int. J. Heat Mass Transf. 28 (1985) 485–495.
[36] J. Kozeny, StizungsberAkad Wiss Wien 136 (1927) 271–306.
[37] P.C. Carman, Trans. Inst. Chem. Eng. 15 (1937) 150–167.
[38] J.H. Nam, K.-J. Lee, G.-S. Hwang, C.-J. Kim, M. Kaviany, Int. J. Heat Mass Transf. 52 (2008) 2779–2791.
[39] A. Corey, Water Resour. (1977) 150.
[40] C.R. Wilke, J. Chem. Phys. 18 (1950) 517–519.
[41] Ch. Hartnig, R. Kühn, Ph. Krüger, J. Schloesser, I. Manke, Fundamental and Development of Fuel Cells 09, Nancy, France, December 2008.
[42] D. Conteau, J. Dillet, C. Bonnet, D. Fünfschilling, M. Weber, F. Lapicque, G. Maranzana, O. Lottin, S. Didierjean, The 20th International Symposium on Transport Phenomena, Victoria, Canada, July 2009, 2009.
[43] J. Ramousse, O. Lottin, S. Didierjean, D. Maillet, J. Power Sources 192 (2009) 435–441.
[44] J. Tafel, Zeit. Physik. Chem. 50-A (1905) 641.
[45] A. Parthasarathy, S. Srinivasan, A.J. Appleby, J. Electroanal. Chem. 39 (1–2) (1992) 101–121.
[46] H. Ju, H. Meng, C.Y. Wang, Int. J. Heat Mass Transf. 48 (7) (2004) 1303–1315.
[47] T.E. Springer, I.D. Raistrick, J. Electrochem. Soc. 136 (6) (1989) 1594–1603.
[48] I.D. Raistrick, Electrochim. Acta 35 (10) (1990) 1579–1586.
[49] F. Jaouen, G. Lindbergh, G. Sundholm, J. Electrochem. Soc. (2002) 437.
[50] R. Madhusudana Rao, D. Bhattacharyya, R. Rengaswamy, S.R. Choudhury, J. Power Sources 173 (1) (2007) 375–393.
[51] J. Ihonen, F. Jaouen, G. Lindbergh, A. Lundblad, G. Sundholm, J. Electrochem. Soc. 149 (4) (2002) 448–454.
[52] K. Broka, P. Ekdunge, J. Appl. Electrochem. 27 (3) (1997) 281–289.
[53] N.P. Siegel, M.W. Ellis, D.J. Nelson, M.R. Von Spakovsky, J. Power Sources 115 (1) (2003) 81–89.
[54] R. Madhusudana Rao, R. Rengaswamy, J. Power Sources 158 (2006) 110–123.
[55] P.J.S. Vie, S. Kjelstrup, Electrochim. Acta 49 (2004) 1069–1077.
[56] G. Maranzana, O. Lottin, T. Colinart, S. Chupin, S. Didierjean, J. Power Sources 180 (2) (2008) 748–754.
[57] K.P. Adzakpa, J. Ramousse, Y. Dubé, H. Akremi, K. Agbossou, M. Dostie, A. Poulin, M. Fournier, J. Power Sources 179 (2008) 164–176.
[58] J. Ramousse, J. Deseure, S. Didierjean, O. Lottin, D. Maillet, J. Power Sources 2 (145) (2005) 416–427.
[59] J.T. Gostick, M.W. Fowler, M.A. Ioannidis, M.D. Pritzker, Y.M. Volfkovich, A. Sakars, J. Power Sources 156 (2006) 375–387.
[60] T. Colinart, A. Chenu, S. Didierjean, O. Lottin, S. Besse, J. Power Sources 190 (2009) 230–240.
[61] F.N. Büchi, S. Srinivasan, J. Electrochem. Soc. 144 (8) (1997) 2767–2772.